HHS Public Access

Author manuscript

Nat Methods. Author manuscript; available in PMC 2017 November 08.

Published in final edited form as:

Nat Methods. 2017 June ; 14(6): 581–583. doi:10.1038/nmeth.4290.

Large-field-of-view imaging by Multi-Pupil Adaptive Optics

Jung-Hoon Park[1,5,†], **Lingjie Kong**[1,6,†], **Yifeng Zhou**[1], and **Meng Cui**[1,2,3,4,*]

[1]School of Electrical and Computer Engineering, Purdue University, West Lafayette, Indiana, USA

[2]Department of Biological Sciences, Purdue University, West Lafayette, Indiana, USA

[3]Integrated Imaging Cluster, Purdue University, West Lafayette, Indiana, USA

[4]Bindley Bioscience Center, Purdue University, West Lafayette, Indiana, USA

Abstract

For *in vivo* deep imaging at high spatiotemporal resolutions, we developed Multi-Pupil Adaptive Optics (MPAO) which enables simultaneous wavefront correction over a large imaging field-of-view. The current implementation improves correction area by nine times over that of conventional methods. MPAO's capability of spatially independent wavefront control further enables 3D nonplanar imaging. We applied MPAO to *in vivo* structural and functional imaging of biological dynamics in mammalian brain.

In vivo optical imaging at high spatiotemporal resolutions is desired in various applications, and is yet challenging due to the refractive index inhomogeneity of biological tissue[1–3]. Adaptive optics (AO) has been applied to correct the optical wavefront distortion[1, 4–14]. However, previous implementations suffer from constrained imaging field-of-view (FOV) and reduced imaging speed as the wavefront distortion varies spatially[7, 11, 15, 16]. Thus a wavefront correction working well for one location may fail to improve or sometimes destroy the image quality for another region. For imaging slow dynamics, we can afford the

*Correspondence and requests for materials should be addressed to Dr. Meng Cui, (+1) 765-494-5486, mengcui@purdue.edu.

[5]Current address: Department of Biomedical Engineering, Ulsan National Institute of Science and Technology, Ulsan, Republic of Korea

[6]Current address: Department of Precision Instrument, Tsinghua University, Beijing, China

†These authors contributed equally to this work.

Data Availability

The data that support the findings of this study are available from the corresponding author upon request.

Code availability

We have uploaded the custom code we used for wavefront measurement.

Author Contributions

M.C. invented MPAO, developed the experimental schemes of wavefront correction and nonplanar imaging, designed the liquid immersion based tunable prism array and supervised the project. J.P. and M.C designed the MPAO based two-photon imaging system. J.P. developed the wavefront measurement and correction algorithm, implemented the imaging system and performed structural imaging of neurons and dynamic imaging of microglia. L.K. designed and performed structural imaging and calcium imaging of neurons, dynamic imaging of microglia, and nonplanar imaging of blood vessels and neurons (data shown in Figs. 1–3 and Supplementary Fig. 6, 9–12). Y.Z. supported the system development, performed structural imaging of neurons and microglia, and assisted the figure preparation. M.C. and L.K. wrote the manuscript with inputs from all authors.

Competing financial interests

The authors declare no competing financial interests.

time-consuming procedure of switching wavefront to image within each small FOV in sequence[11, 13]. However, this method fails for many applications where large-scale, high-throughput imaging is required (Supplementary Note 1). New approaches that can provide simultaneous wavefront correction over a large FOV and hence enable imaging at the highest throughput limited only by the sample or the imaging hardware are urgently needed. Here, we present such a solution, Multi-Pupil Adaptive Optics (MPAO), and demonstrate its performance for high-throughput large-FOV *in vivo* imaging of mammalian brain.

The essence of MPAO is the simultaneous position-dependent wavefront correction. In conventional AO, a single spatial light modulator (SLM) is placed on the pupil plane of the objective lens. Therefore, the wavefront correction measured from one region is applied to the entire image (Fig. 1a), which however only improves the imaging performance within a limited FOV. If we instead apply the wavefront averaged over multiple regions, the resulting correction is not ideal for any region (Fig. 1b). In MPAO, we position a multi-facet prism array on the sample plane, which applies angular tilt to the optical beam (Fig. 1c). In the pupil plane, angular tilt becomes pupil image translation. Thus, we construct an array of pupil images (plane 2 in Fig. 1c), each corresponding to one region on the sample plane. We use a SLM to display an array of wavefront profiles and achieve simultaneous independent correction for all regions. Using a second prism array of complementary angular tilt, we cancel the applied tilt and obtain a fully corrected image.

We implemented MPAO with two-photon microscopy (TPM) by using a nine-facet prism array forming a 3×3 array of pupil images on a SLM (Supplementary Fig. 1). Each prism segment corresponded to a 150×150 μm^2 area and thus the 3×3 prism array provided a 450×450 μm^2 FOV (Supplementary Fig. 2). The prism segment's dimension was determined experimentally to provide a compromise between FOV and correction quality (Supplementary Fig. 3 and Note 2). Before imaging, we employed Zernike mode based optimization to determine the correction wavefront[1, 8] (Methods). Using MPAO, we measured the wavefront for all nine regions simultaneously and then performed resonant-Galvo based TPM.

We demonstrate the applications of MPAO for *in vivo* mammalian brain imaging. The first application is the high-resolution dynamic imaging of microglia, the resident immune cells. For wavefront measurement, we used the fluorescence of green fluorescence protein (GFP) in the microglia of CX3CR1-GFP mice as the feedback. Correcting only the system induced aberration (system correction) resulted in marginal improvement (Fig. 1d). Using MPAO to correct both the system and the tissue induced aberration (full correction), we obtained clear images across the entire FOV (Fig. 1e, Supplementary Fig. 4). The independent and parallel correction (Fig. 1f) improved both image brightness and resolution (Figs. 1g–1j). To quantify the resolution, we measured the cross-section of the microglia's fine processes (Figs. 1i and 1j), whose full-width-at-half-maximum was 0.54 ± 0.20 μm (n = 40) with system correction and 0.36 ± 0.02 μm (n = 40) with full correction, close to the theoretical limit (0.34 μm for 935 nm laser and 1.04 excitation numerical aperture [NA]).

We compare MPAO with the two implementations of conventional AO shown in Figs. 1a and 1b. In one implementation (named Full single), we aimed to get the same image quality

as that of MPAO. Experimentally, we used the image within one of the nine segments of MPAO for wavefront measurement. The wavefront was identical to the one employed by MPAO for the same segment, which provided improvement only within a limited FOV (Supplementary Fig. 4 and Video 1). In the other implementation (named Full average), we aimed to obtain the same FOV size as that of MPAO. Experimentally, we used the image over the entire FOV as the feedback to optimize the wavefront. Compared to the individually optimized wavefront in MPAO, the obtained wavefront was smoother (Fig. 1f), which however provided only minor improvement in image quality (Supplementary Fig. 4, Video 1 and Note 3).

Next, we demonstrate dynamic large-FOV volumetric imaging of microglia in the resting (Supplementary Fig. 5 and Video 2) and activated states. Experimentally, we introduced tissue damage by laser ablation and monitored microglia's response by time-lapse volumetric imaging (Fig. 1k, Supplementary Fig. 6 and Video 3).

Dendritic spines are the storage sites of synaptic strength, whose plasticity in shape, size, and number underpins memory and learning. High-resolution *in vivo* imaging of dendritic spines is therefore of great importance in neuroscience. Due to brain tissue induced aberration, most high-resolution studies are constrained to 200–300 μm in depth. Using MPAO, we can perform high-resolution large FOV imaging at a depth of up to ~ 650 μm. We employed Thy1-YFP mice which express yellow fluorescence protein (YFP) in a subset of layer 5 neurons. Using MPAO, we were able to record high-resolution volumetric images of the neuronal network (Supplementary Fig. 7a and Video 4). We show the maximum intensity projections from two stacks, each of 50 μm thickness (Supplementary Figs. 7b and 7c, centered at the depth of 75 and 325 μm, respectively). The zoomed-in images provide a clear view of the dendritic structures resolved by MPAO. If the correction wavefront optimized for one region was applied to all other regions as in conventional AO, the improvement FOV would be reduced even at moderate depth (Supplementary Fig. 8). With full correction, we could resolve spines on the basal dendrites of layer 5 neurons at large depths (623 μm in Supplementary Fig. 7d, and 653 μm in Supplementary Fig. 9), which were rather blurry with only system correction applied.

Calcium imaging has been widely employed for large-scale recording of neuronal activity, which demands both speed and image quality. Especially for imaging fine structures, it is important to have a high-quality focus, which not only ensures efficient excitation but also reduces the signal contamination by surrounding neuropils[17]. Previous implementations of AO have demonstrated improved focus quality. However, the improvement was confined to a small FOV, inadequate for large-scale recording. Using MPAO, we overcame this limitation by simultaneously correcting wavefront aberrations in parallel and achieved large-FOV high-speed imaging. We employed Thy1-GCaMP6s (line GP 4.3) mice which express calcium indicator GCaMP6s in subsets of neurons, and monitored the spontaneous neuron activity in the primary visual cortex. As the fluorescence from GCaMP inherently fluctuates due to the spontaneous neuron activity, we introduced a stable red fluorescence signal for wavefront measurement by staining astrocytes with SR101, which can be excited at the same wavelength (935 nm) as GCaMP. After the wavefront measurement, we performed calcium imaging at 15 Hz frame rate. For comparison, we show the images of neurons and astrocytes

both with full and with system wavefront correction (Fig. 2). With full correction, the fine processes of astrocytes (Figs. 2a–2d) and the neurites (Figs. 2e and 2f) can be resolved. We extracted the calcium transients from several neurites (Figs. 2g–2i, Supplementary Fig. 10 and Video 5), to show the superior signal-to-noise-ratio provided by MPAO.

With the independent wavefront control, MPAO can also enable non-planar microscopy, which brings 3D features at different depths into the same imaging plane for high-speed measurement (Supplementary Fig. 11). Here, we show the nonplanar imaging of neurovasculature regulation (Fig. 3). We applied different defocusing wavefront to the nine pupils, which independently shifted the focal planes in the axial direction to reach the blood vessels of interest. We then performed wavefront correction using the YFP expressing neurons as feedback (Supplementary Fig. 12 and Video 6). The combined defocusing and aberration correction enabled simultaneous measurement of the dilation of the 3D vasculature network at 7.65 Hz (Supplementary Video 7). With the mice under mild anesthesia, we observed synchronized dilation (Fig. 3e).

In summary, we demonstrate the performance of MPAO in high-speed large-FOV imaging. With the correction wavefront applied, the imaging procedure is the same as conventional systems but with all regions of the FOV simultaneously corrected. The independent wavefront control further enables high-speed nonplanar microscopy. The simultaneous large-FOV correction will be indispensable for high spatiotemporal resolution measurements in many biological systems (Supplementary Note 4).

Methods

System design

We designed the imaging system by combining MPAO with TPM (Supplementary Fig. 1). The laser source was a tunable femtosecond laser (Coherent Chameleon Vision and Discovery) with built-in dispersion compensation capability. The excitation wavelength was 935 nm. We expanded the laser beam to overfill the 5 mm aperture of the dual-axis resonant Galvo scanning mirror system (Cambridge Technology) and aligned the polarization along the working axis of the SLM (Hamamatsu, X 10468-07). We used a pair of telecentric relay lenses (focal length 150 and 110 mm) in a 4-f configuration to image the Galvo mirror onto the SLM. In the common focal plane of the two relay lenses, we positioned the first prism array, which established nine (3×3) pupil images on the SLM. With the 5 mm aperture resonant Galvo scanner, the size of each pupil image was 3.67 mm in diameter on the SLM (183 SLM pixels across the pupil diameter). It is worth noting that the prism array did not split the pupil into nine images. Instead, there was only a single pupil image on the SLM for any point on the sample plane. The second pair of telecentric relay lenses (focal length 110 and 500 mm) imaged the SLM onto the back focal plane of the objective lens (Nikon 25× NA 1.1). We also positioned a second prism array that offered complementary angular tilt at the common focal plane of the second relay lens pair. The complementary prism array canceled the angular tilt applied by the first prism array and recombined the 3×3 pupil array back into a single pupil image (16.7 mm in diameter).

Prism design

The key component of MPAO is the element that can apply angular tilt to the light beam, which can be achieved by either reflection, such as by a multi-facet mirror ball, or transmission, using the multi-facet prism array of this work. The reflective configuration is independent of wavelength and is completely free from chromatic angular chirp, making it most appropriate for applications involving very large optical bandwidth such as fluorescence emission in wide-field recording. However, the reflection design allows no adjustment of the beam tilting angles. To permit matching the requirement for objectives of different NA, we developed the transmission design with customized multi-facet prisms (CPG Optics, segment size = 9.375 mm, facet angle = 0, ± 23.4, ± 31.5 degree) and immersed the prism in refractive index liquid (Supplementary Fig. 2). With such a design, we gained the flexibility of adjusting the tilt angle. In fact, we used the same fused silica (n = 1.451) prism array and selected different immersion liquids (n = 1.529 and 1.374) to form both of the two complementary prim arrays. It is worth noting that the spectral angular chirp induced by the prism array was negligible for the ~100 fs duration laser pulses for two reasons. First, the applied angular tilt was a very small angle equal to the angular spread of the optical beam. This is very different from the dispersion prism used in pulse compressors, which produces a huge angular deviation. Second, we chose low dispersion materials, fused silica and low refractive index immersion liquid. To hold the prism array and the immersion oil, we attached the prism array to an optical window using UV-epoxy, fixed the optical window to the bottom of a lens tube (SM2L10, Thorlabs), filled in the immersion oil, and covered the oil with the second optical window. We applied UV-epoxy to seal the interface between the lens tube and the two optical windows (one on each side of the prism array).

Sensorless wavefront measurement

A variety of wavefront measurement methods can be applied to the MPAO system. In this work, we employed the Zernike mode based sensorless method for its compatibility with the resonant Galvo based TPM and the update rate of liquid crystal SLM. Essentially, we adjusted the coefficient of each Zernike mode and observed the variation of certain image metrics. In this work, we chose image intensity as the optimization metric, which we found robustly yielded the aberration correction wavefront. Typically, we used 7–9 data points (i.e. changed the amount of each Zernike mode to 7–9 different values), extracted the image metric at each data point, and applied Gaussian fitting to the metric curve (metric value vs. amount of Zernike mode) to find the center of the Gaussian curve, which returned the coefficient of the needed Zernike mode correction (see Supplementary Software). As an example, we show the wavefront measurement result (Supplementary Fig. 13) obtained during the microglia imaging (Fig. 1). Typically, we measured up to 60 orders of Zernike modes.

The employed objective lens (Nikon 25× NA 1.1) can provide spherical aberration correction. Experimentally, we tuned the correction collar such that the cover glass aberration was minimized. We then performed a system aberration measurement to determine the remaining aberration. After this step, the overall imaging system (including the cover glass) was fully corrected. For *in vivo* measurements, we encountered additional aberrations caused by the biological tissue. The full correction therefore contained both the

system correction and the tissue correction. When we made image comparisons, we compared the results with full correction and with system correction. We have also compared MPAO enabled full correction with other conventional AO methods (Supplementary Fig. 4 and Note 3). For 3D volumetric imaging, the wavefront aberrations were measured at different depths in 50 μm steps (Supplementary Fig. 14).

Nonplanar imaging

Using MPAO, we could flexibly add defocusing wavefront to each pupil and axially shift features from different depths onto a single 2D image plane for high-speed recording. Experimentally, we first added the defocusing wavefront to reach the desired depth and then measured the correction wavefront there. Thus, each region was still optimally corrected while being at different depths. The defocusing wavefront, $dcos(\theta)n$, is a function of the axial shift (d), the incident beam angle (θ) and the refractive index of the immersion medium (n).

Animal preparation and *in vivo* imaging

All procedures involving mice were approved by the Animal Care and Use Committees of Purdue University. We used female mice of 8 weeks to 6 months old without randomization or blinding.

We used Thy1-YFP (H line) (JAX No.: 003782) and CX3CR1$^{GFP/GFP}$ (JAX No.: 005582) transgenic mice for structural imaging of neurons and microglia, respectively. During the craniotomy above S1 cortex (circular, diameter Φ=3 mm), we placed the mice on a soft heating plate and kept them under isoflurane anesthesia (2–2.5% for induction, 1.5–2% during surgery). After that, we applied 1% agarose on the cranial windows, and cemented the coverslips (circular, Φ =5 mm, 170 μm thick) and the custom titanium head posts to the skull. Then we placed the anesthetized (1–1.5 % isoflurane) mice under the microscope for imaging, while keeping the mice warm. For the dynamic imaging of activated microglia, we introduced laser ablation as described in the literature[18].

We used Thy1-GCaMP6s[19] (line GP4.3) (JAX No.: 024275) transgenic mice for functional imaging of neural activity. We prepared the mice using the same procedures as for structural imaging, except that (1) we made the craniotomy above V1 cortex (centered 2.7 mm left, and 0.2 mm anterior to the Lambda suture); (2) before placing agarose and installing the window, we applied SR101 solution (10 μM) onto the cerebral cortex for 5–8 min to stain the astrocytes[20]; (3) during imaging, we kept the mice under low anesthesia (~0.5 % isoflurane) to have more active spontaneous neural activities.

We used Thy1-YFP (H line) (JAX No.: 003782) for the nonplanar microscopy of neurovasculature regulation. We prepared chronic windows above S1 cortex using the same procedures as in structural imaging. Before imaging, we performed retro-orbital injection of Texas-Red to label the blood plasma for monitoring vasculature dilations. During the imaging, the mice were under mild anesthesia (~1 % isoflurane).

For each type of imaging experiments, we typically used three or more mice. The variation between different mice is minor. The surgery procedure of craniotomy is important to minimize damage to the dura, which ensures a consistent imaging result.

Detailed imaging parameters are summarized in Supplementary Table 1.

Data analysis

We rendered the 3D data using Amira (FEI), and displayed the 2D images with ImageJ (NIH). For function imaging data, we selected regions of interest using a semi-automated algorithm[21].

Statistics

To quantify the spatial resolution in Fig. 1, we measured the FWHM from 40 locations and reported the mean value and the standard deviation.

Supplementary Material

Refer to Web version on PubMed Central for supplementary material.

Acknowledgments

This work was funded by NIH (1U01NS094341-01) and Purdue University. The authors thank W. Gan for valuable discussion and advice, thank G. Holtom and B. Wei for the help on manuscript preparation, and thank Howard Hughes Medical Institute for the equipment support. J.P. thanks NRF-2016R1C1B2015130 for the support during the manuscript preparation and L.K. thanks NSFC No. 61327902 for the support during manuscript revision.

References

1. Booth MJ, Neil MAA, Juskaitis R, Wilson T. Adaptive aberration correction in a confocal microscope. Proceedings of the National Academy of Sciences of the United States of America. 2002; 99:5788–5792. [PubMed: 11959908]
2. Vellekoop IM, Mosk AP. Focusing coherent light through opaque strongly scattering media. Optics Letters. 2007; 32:2309–2311. [PubMed: 17700768]
3. Popoff S, Lerosey G, Fink M, Boccara AC, Gigan S. Image transmission through an opaque material. Nature Communications. 2010; 1:81.
4. Roorda A, Williams DR. The arrangement of the three cone classes in the living human eye. Nature. 1999; 397:520–522. [PubMed: 10028967]
5. Paterson C, Munro I, Dainty J. A low cost adaptive optics system using a membrane mirror. Optics Express. 2000; 6:175–185. [PubMed: 19404349]
6. Marsh PN, Burns D, Girkin JM. Practical implementation of adaptive optics in multiphoton microscopy. Optics Express. 2003; 11:1123–1130. [PubMed: 19465977]
7. Kam Z, Kner P, Agard D, Sedat JW. Modelling the application of adaptive optics to wide-field microscope live imaging. Journal of Microscopy-Oxford. 2007; 226:33–42.
8. Zeng J, Mahou P, Schanne-Klein MC, Beaurepaire E, Débarre D. 3D resolved mapping of optical aberrations in thick tissues. Biomedical optics express. 2012; 3:1898–1913. [PubMed: 22876353]
9. Ji N, Milkie DE, Betzig E. Adaptive optics via pupil segmentation for high-resolution imaging in biological tissues. Nature Methods. 2010; 7:141–147. [PubMed: 20037592]
10. Tao X, et al. Adaptive optics microscopy with direct wavefront sensing using fluorescent protein guide stars. Optics Letters. 2011; 36:3389–3391. [PubMed: 21886220]

11. Tang J, Germain RN, Cui M. Superpenetration optical microscopy by iterative multiphoton adaptive compensation technique. Proceedings of the National Academy of Sciences of the United States of America. 2012; 109:8434–8439. [PubMed: 22586078]
12. Adie SG, Graf BW, Ahmad A, Carney PS, Boppart SA. Computational adaptive optics for broadband optical interferometric tomography of biological tissue. Proceedings of the National Academy of Sciences of the United States of America. 2012; 109:7175–7180. [PubMed: 22538815]
13. Wang K, et al. Rapid adaptive optical recovery of optimal resolution over large volumes. Nature Methods. 2014; 11:625–628. [PubMed: 24727653]
14. Čižmár T, Dholakia K. Exploiting multimode waveguides for pure fibre-based imaging. Nature communications. 2012; 3:1027.
15. Park JH, Sun W, Cui M. High-resolution in vivo imaging of mouse brain through the intact skull. Proceedings of the National Academy of Sciences of the United States of America. 2015; 112:9236–9241. [PubMed: 26170286]
16. Mertz J, Paudel H, Bifano TG. Field of view advantage of conjugate adaptive optics in microscopy applications. Applied Optics. 2015; 54:3498–3506. [PubMed: 25967343]
17. Yasuda R, et al. Imaging calcium concentration dynamics in small neuronal compartments. Science's STKE: signal transduction knowledge environment. 2004; 2004:l5.
18. Davalos D, et al. ATP mediates rapid microglial response to local brain injury in vivo. Nature neuroscience. 2005; 8:752–758. [PubMed: 15895084]
19. Dana H, et al. Thy1-GCaMP6 transgenic mice for neuronal population imaging in vivo. PloS one. 2014; 9:e108697. [PubMed: 25250714]
20. Nimmerjahn A, Kirchhoff F, Kerr JN, Helmchen F. Sulforhodamine 101 as a specific marker of astroglia in the neocortex in vivo. Nature Methods. 2004; 1:31–37. [PubMed: 15782150]
21. Chen TW, et al. Ultrasensitive fluorescent proteins for imaging neuronal activity. Nature. 2013; 499:295–300. [PubMed: 23868258]

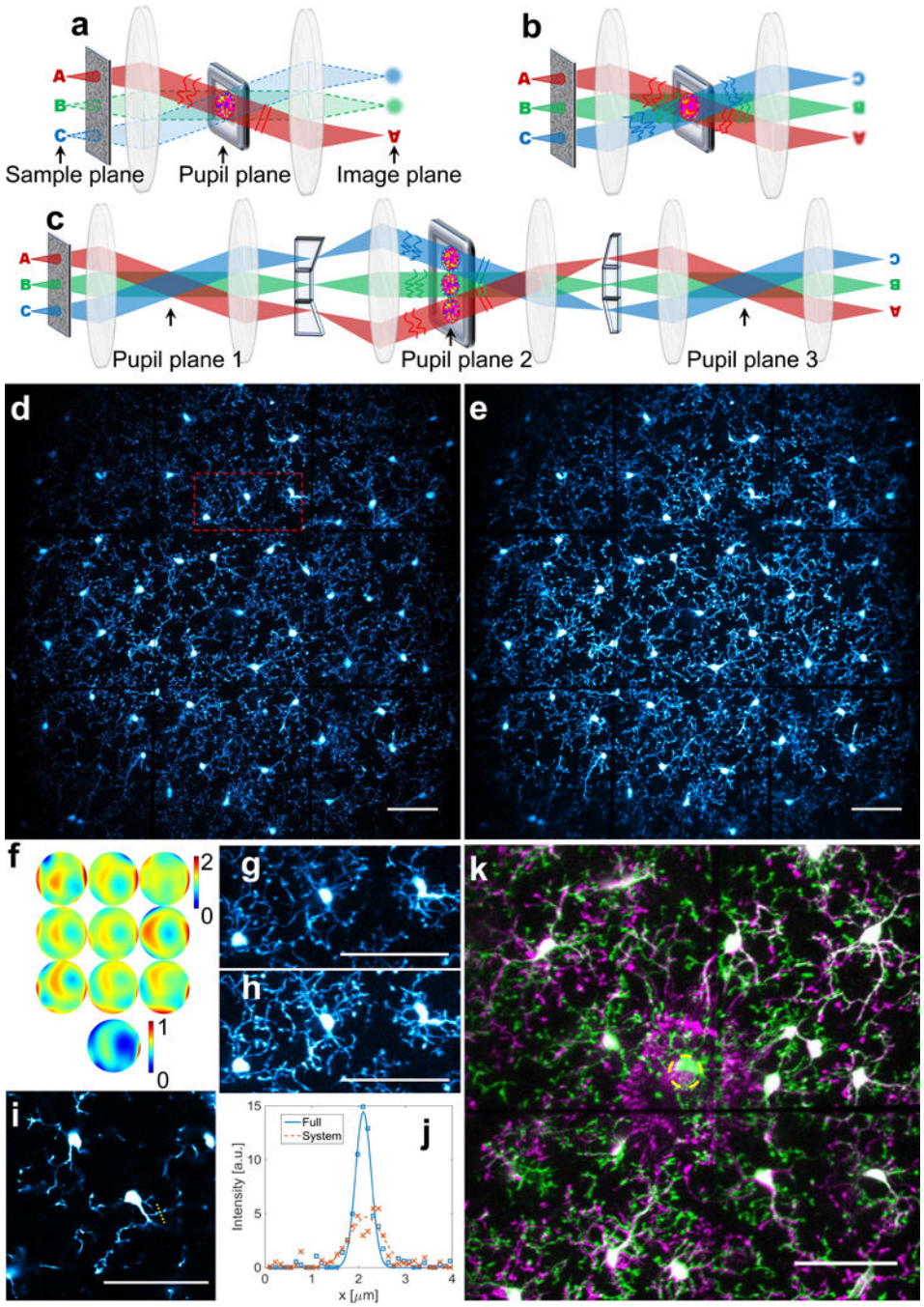

Figure 1. The design of MPAO and the application for imaging microglia dynamics

(**a**, **b**) Conventional AO with the wavefront correction measured for one location and averaged over multiple locations applied to the entire FOV, respectively. (**c**) The design of MPAO that achieves simultaneous position-dependent correction. (**d**, **e**) Maximum intensity projections (MIPs) along *z* axis of a 40 μm thick image stack (330–370 μm under the dura) acquired with system and with full wavefront correction, respectively. Scale bar: 50 μm. (**f**). The nine wavefront profiles measured by MPAO for the 3×3 image segments and the averaged wavefront which was measured by using the entire image FOV as the feedback.

The wavefront amplitude is scaled to the laser wavelength of 935 nm. (**g**, **h**) The zoomed-in view of the area enclosed by the red dashed box in **a**. Scale bar: 20 μm. (**i**, **j**) The *x*-*y* image of the fine processes of microglia from the central image segment and the cross-section plot with Gaussian fitting (along the yellow dashed line). (**k**) Microglia dynamics before and after activation by laser ablation, shown in green and magenta respectively. Green: t_0; magenta: t_0+56 min. Laser ablation was applied at t_0+25 min. The ablation site is labeled by the yellow dashed circle. Scale bar: 50 μm. The data shown in this figure is representative of three data sets.

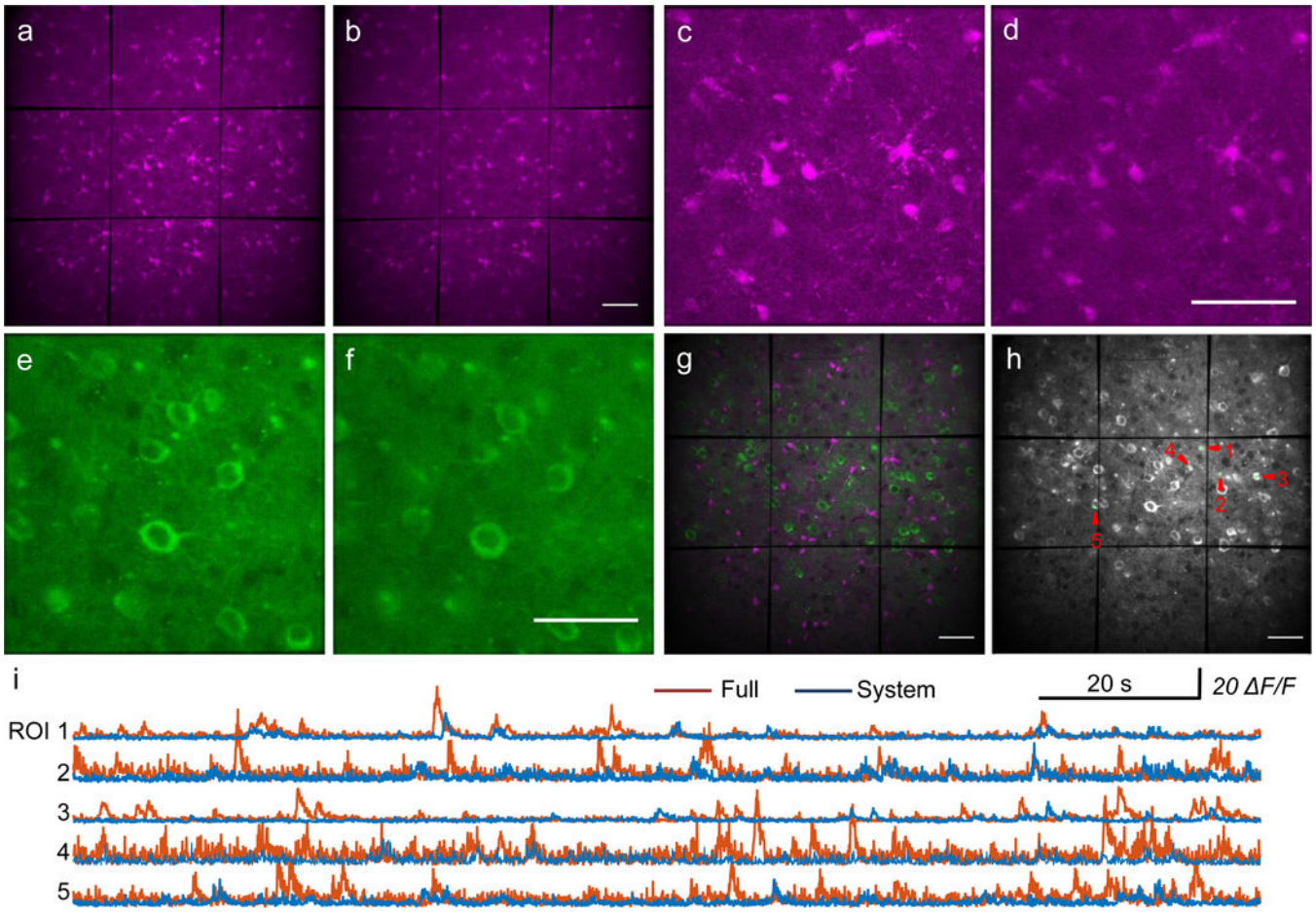

Figure 2. Calcium imaging of neurons at a depth of 450 μm with MPAO

(**a**, **b**) MIPs along *z* of SR101 stained astrocytes at 436–465 μm under the dura with full and with system correction, respectively. (**c**, **d**) Zoomed-in view of the central 150 × 150 μm^2 area in **a** and **b**. (**e**, **f**) Standard deviation of the time-lapse images of GCaMP6s-expressing neurons with full and with system correction, respectively. The images **c**–**f** were from the same area. (**g**) Composite view of astrocytes (magenta) and neurons (green) at a depth of 450 μm. (**h**) Regions of interest (ROIs) for computing calcium transients. (**i**) Calcium transients with full and with system correction. Scale bars: 50 μm. The data shown in this figure is representative of four data sets.

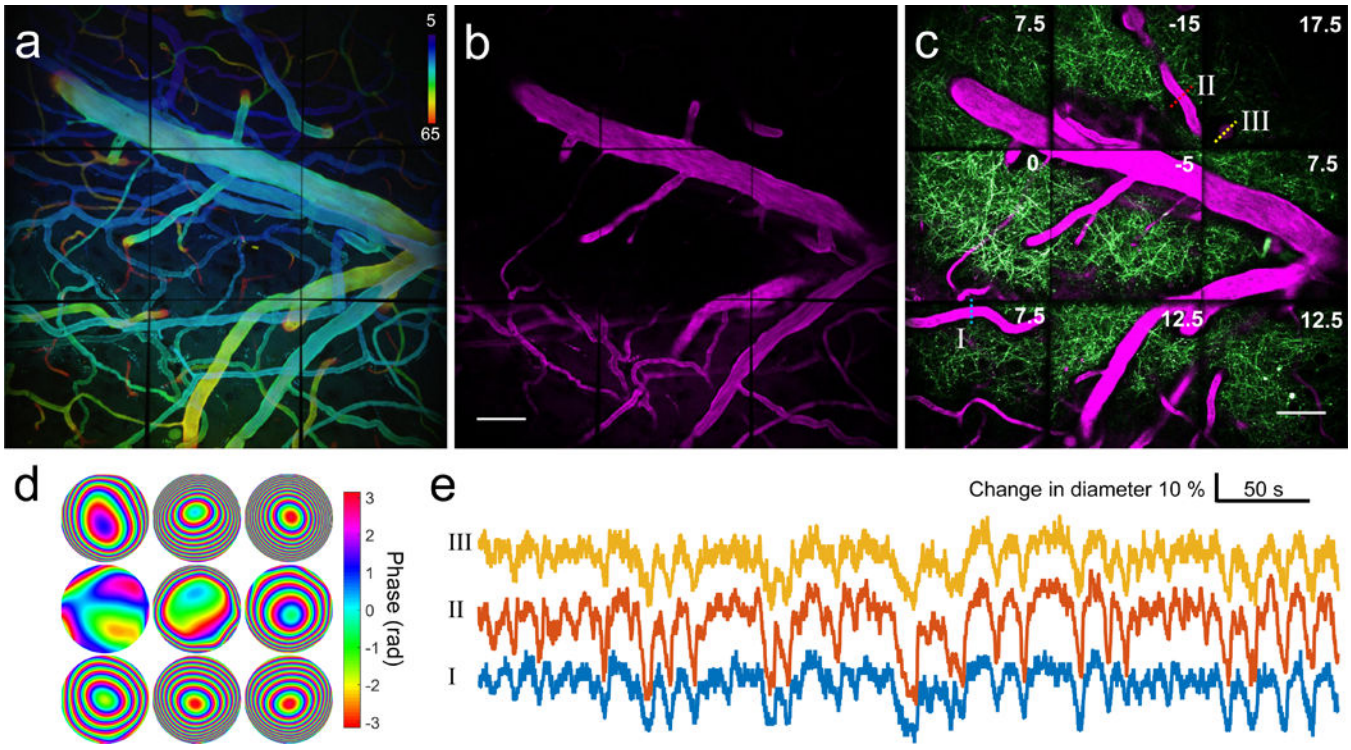

Figure 3. Nonplanar microscopy of 3D vasculature dynamics

(**a**) Vasculature network at 6–65 μm depth under the dura with the depth color-encoded. (**b**) Planar imaging of blood vessels at the depth of 35 μm. (**c**) Nonplanar imaging of blood vessels and neural dendrites, with the relative depth shown in each image segment in micron. The central segment was at the depth of 35 μm. Magenta: Texas-Red labeled blood plasma; Green: YFP expressing neural dendrites. (**d**) Wavefront applied to the pupil array, which shifted the focal planes and corrected tissue induced aberration. (**e**) Synchronized dilation of three blood vessels at different depths. Their corresponding positions are marked in **c** with the dotted lines indicating the position of measurement. Vessel III is a vertically penetrating vessel originating from Vessel II as shown by the volumetric view in **a**. The data shown in this figure is representative of three data sets.